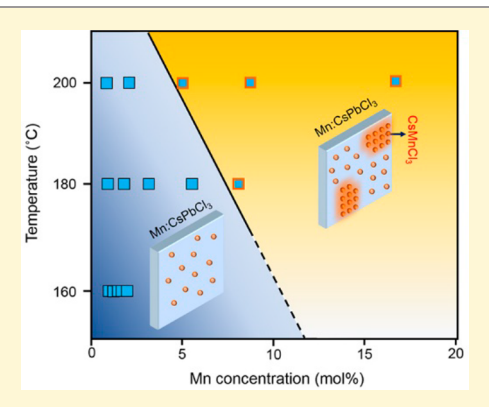


# Complete Dopant Substitution by Spinodal Decomposition in Mn-Doped Two-Dimensional CsPbCl<sub>3</sub> Nanoplatelets

Zhi-Jun Li, Elan Hofman, Andrew Hunter Davis, Alex Khammang, Joshua T. Wright, Boris Dzikovski, Robert W. Meulenberg, and Weiwei Zheng\*, leng\*,

# Supporting Information

ABSTRACT: The introduction of dopants plays a key role in the physical properties of semiconductors for optoelectronic applications. However, doping is generally challenging for nanocrystals (NCs), especially for two-dimensional (2D) NCs, due to the self-annealing effect and high surface energies required for dopant addition. Here, we report an efficient doping strategy for Mn-doped 2D CsPbCl<sub>3</sub> (i.e., Mn:CsPbCl<sub>3</sub>) nanoplatelets (NPLs) through a postsynthetic solvothermal process. While the original lightly doped 2D Mn:CsPbCl<sub>3</sub> NPLs were obtained from growth doping, higher Mn doping efficiencies were achieved through diffusion doping under pressure-mediated solvothermal conditions, resulting in enhanced Mn photoluminescence (PL). Surprisingly, a new CsMnCl<sub>3</sub> phase with complete dopant substitution by spinodal decomposition was observed with extended solvothermal treatment, which is confirmed by powder X-ray diffraction, X-ray absorption fine structure, and electron paramagnetic



resonance. Compared with Mn:CsPbCl<sub>3</sub> NPLs, the pure CsMnCl<sub>3</sub> NPLs give rise to shorter Mn PL lifetime, which is consistent with the short Mn-Mn distance within CsMnCl<sub>3</sub> NPLs. This work provides an efficient strategy for doping inside NCs as well as new insights on the dopant concentration-dependent structural and optical properties of perovskite NCs.

## **■** INTRODUCTION

Cesium lead halide perovskite (e.g., CsPbX<sub>3</sub>, X = Cl<sup>-</sup>, Br<sup>-</sup>, I<sup>-</sup>, or mixtures thereof) nanocrystals (NCs) are a new class of semiconductor materials with promising applications in optoelectronics, such as light-emitting diodes, photodetectors, and solar cells. 1-7 Recently, two-dimensional (2D) perovskite nanoplatelets (NPLs) have drawn significant interest because of their ultranarrow absorption and emission peaks, excellent charge transport properties, and large lateral sizes that could be easily integrated into devices.  $^{8-10}$  The intentional incorporation of transition metal ions as dopants offers exciting opportunities to endow perovskite NCs with novel optical, electronic, and magnetic functionalities. 10-19 So far, Mn-doped CsPbCl<sub>3</sub> and CsPbBr<sub>3</sub> nanocubes or 2D NPLs by substitutional incorporation of the dopant ion on Pb<sup>2+</sup> sites have been synthesized, 9,10,13-21 which exhibited Mn emission resulting from the energy transfer from exciton to Mn<sup>2+</sup> ion.

There have been many synthetic methods developed for transition metal ion doped II-VI NCs, such as using singlesource precursors, 22,23 nucleation doping, 24 growth doping, 25,26 ion exchange, and diffusion. 27-30 It has been shown, however, that doping of Mn<sup>2+</sup> into perovskite NCs is difficult most likely due to the large size mismatch between the Mn<sup>2+</sup>

(97 pm) dopant and the Pb<sup>2+</sup> (133 pm);<sup>14</sup> therefore, the doping efficiency can be rather low even with very high concentrations of dopant precursor introduced in the synthesis. 14-16 For example, Parobek et al. obtained 0.2% doping in CsPbCl<sub>3</sub> nanocubes by using extremely high concentrations of Mn precursor with Mn:Pb in a 3:2 mol ratio. 16 In addition, the high activation energies for the formation of cation vacancies and the lack of interstitial sites for ion diffusion in perovskite NCs12,31 could account for the very slow cation diffusion compared to anion diffusion in perovskites. 19,32,3 Furthermore, despite doped 0D NCs being widely studied, doped anisotropic NCs, especially 2D NCs, have been less explored. Therefore, developing new strategies for efficient incorporation of dopants in advance-shaped perovskite NCs is required.

Here, we introduce a facile solvothermal method for efficient Mn doping in 2D CsPbCl<sub>3</sub> nanoplatelets (NPLs). This strategy not only allows us to improve the doping efficiency through diffusion doping under solvothermal conditions but also leads

Received: June 23, 2018 Revised: August 23, 2018 Published: August 23, 2018

Department of Chemistry, Syracuse University, Syracuse, New York 13244, United States

<sup>\*</sup>Laboratory for Surface Science and Technology and Department of Physics and Astronomy, University of Maine, Orono, Maine 04469, United States

<sup>\*</sup>Department of Physics, Illinois Institute of Technology, Chicago, Illinois 60616, United States

<sup>§</sup>National Biomedical Center for Advanced Electron Spin Resonance Technology, Ithaca, New York 14853, United States

to a gradual phase segregation of pure CsMnCl<sub>3</sub> from Mn:CsPbCl<sub>3</sub> NPLs by spinodal decomposition. The increased doping concentration could lead to higher Mn photoluminescence (PL) quantum yields (QY) and stronger Mn-Mn interactions. The new CsMnCl<sub>3</sub> phase with complete dopant substitution is evidenced by powder X-ray diffraction (XRD) analysis and further supported through a newly distinguished electron paramagnetic resonance (EPR) peak and X-ray absorption fine structure (XAFS) analysis. Transmission electron microscopy (TEM) images indicate that the 2D morphology and size of the NPLs are unchanged before and after phase segregation under solvothermal conditions. While phase segregation from a uniform crystal via spinodal decomposition can occur in the bulk materials, this is the first report on the spinodal decomposition in doped 2D NCs while preserving the original NC shape, to the best of our knowledge. This doping strategy offers a unique platform to investigate the change in structure and phase of doped 2D perovskite NCs and could offer new possibilities for property engineering of doped NCs.

## RESULTS

In this study, 2D Mn-doped CsPbCl<sub>3</sub> (i.e., Mn:CsPbCl<sub>3</sub>) perovskite NPLs were prepared via a two-step synthetic method, as shown in Figure 1a. In the first step, we synthesized

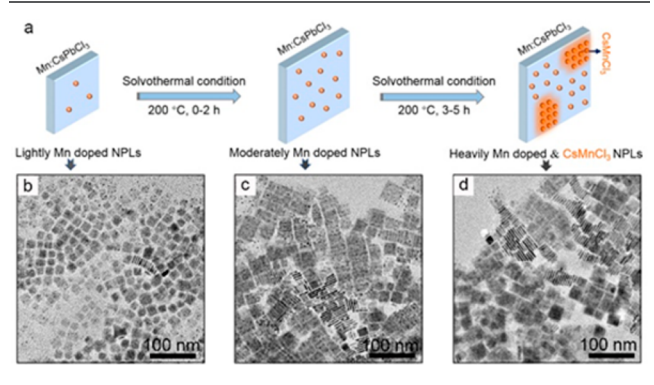


Figure 1. (a) Schematic of the formation of Mn-doped 2D CsPbCl $_3$  perovskite NPLs via a hot-injection method followed by solvothermal growth for heavily Mn-doped larger CsPbCl $_3$  NPLs and CsMnCl $_3$  inclusion after phase segregation. (b) TEM images of 2D Mn:CsPbCl $_3$  perovskite NPLs synthesized in three-neck round-bottom flasks under atmospheric pressure. TEM images of larger 2D Mn:CsPbCl $_3$  perovskite NPLs grown in Teflon-lined autoclaves after solvothermal treatment of (c) 3 and (d) 5 h.

lightly doped 2D Mn:CsPbCl<sub>3</sub> NPLs by the injection of Csoleate into an oleic acid and oleylamine solution containing PbCl<sub>2</sub> and MnCl<sub>2</sub> (80%, mol % to Pb) at 120 °C. Subsequently, the stock solution was transferred into a Teflon-lined stainless-steel autoclave to grow heavily doped Mn:CsPbCl<sub>3</sub> NPLs under solvothermal conditions at 200 °C for 2–5 h. The detailed synthesis is given in the Experimental Section. The TEM image of samples before solvothermal treatment (Figure 1b) shows 2D Mn:CsPbCl<sub>3</sub> with a few NPLs lying perpendicular to the TEM grid via face-to face assembly with averge edge lengths and thicknesses of the NPLs as 20  $\pm$  5 and ~3.0  $\pm$  0.3 nm, respectively. The phenomena of self-assembly of 2D NPLs on TEM grids is similar to prior reports of CsPbBr<sub>3</sub> NPLs<sup>34</sup> and Mn-doped 2D CsPbCl<sub>3</sub> NPLs.  $^{10,35}$  It should be noted that the thin NPLs can be partially destroyed

by the high-energy electron beam and form dark metallic lead particles during TEM measurements.  $^{10,35-37}$ 

After solvothermal treatment (2–5 h) of the stock solution obtained in the first step, slightly larger Mn-doped 2D CsPbCl<sub>3</sub> NPLs were obtained with lateral size  $\sim$ 40 nm (Figure 1c–d, Figure S1), which are nearly doubled compared with the 2D NPLs before solvothermal treatment (Figure 1b). The larger NPLs predominately lie flat on the TEM grid with a few lying perpendicular to the TEM grid. While the lateral dimensions increase by nearly double, the thickness of the CsPbCl<sub>3</sub> NPLs is almost the same,  $\sim$ 3.0  $\pm$  0.3 nm (Figure 1c–d, Figure S1). The nearly doubled lateral dimensions with similar thickness of the 2D NPLs after solvothermal growth suggest that the larger 2D NPLs were formed as the result of oriented attachment of the small 2D NPLs under solvothermal conditions.

Although the NPLs prepared at different solvothermal treatment time (2-5 h) exhibit similar 2D morphology and size (Figure 1c-d, Figure S1), inductively coupled plasma optical emission spectroscopy (ICP-OES) measurements indicate the concentration of Mn<sup>2+</sup> in the NPLs significantly increased along with the solvothermal treatment time (Figure 2c and Table S1). The Mn<sup>2+</sup> concentration dramatically increases from 1.0% (mol % to Pb) of the lightly 2D Mn:CsPbCl<sub>3</sub> NPLs to 2.3%, 5.0%, 8.8%, and 16.8% (mol % to Pb) for the NPLs after solvothermal treatment for 2, 3, 4, and 5 h, respectively. While growth doping could account for the lightly doped 2D Mn:CsPbCl<sub>3</sub> NPLs from the hot-injection method, 38,39 it is believed that diffusion doping by the substitution of host ions by added dopant ions via ion exchange<sup>12</sup> leads to the higher doping efficiency of the Mn:CsPbCl<sub>3</sub> NPLs under solvothermal conditions. While diffusion doping has been reported in doped II-VI semi-conductor NCs<sup>28,40</sup> and perovskite quantum dots, this is the first evidence of diffusion doping in 2D perovskite NCs to the best of our knowledge. 19

To understand how the increasing Mn concentration affects the structural and optoelectronic properties of the 2D NPLs, XRD, EPR, XAFS, and optical measurements were performed. XRD confirms the as-prepared 2D Mn:CsPbCl<sub>3</sub> NPLs before solvothermal treatment (denoted as "0 h" sample in Figures 2-6) possess the crystalline structure of cubic CsPbCl<sub>3</sub> (Figure 2a). A magnified view of the (200) peak at  $\sim 32^{\circ}$ reveals that the peak is slightly shifted to higher angles compared to undoped cubic CsPbCl<sub>3</sub> (Figure 2b-c). In addition, a continuous shift of the (200) peak toward higher angle is observed with increasing the solvothermal treatment time from 0 to 5 h (a total of 0.32° shift). This shift indicates a higher Mn incorporation and progressive lattice contraction due to the substitution of larger Pb<sup>2+</sup> ions (133 pm) by the isovalent, yet smaller, Mn<sup>2+</sup> ions (97 pm). Similar results were also obtained in Mn-doped CsPbCl<sub>3</sub> NCs with increasing Mn incorporation. 15,17,41 These observations are consistent with XAFS measurements taken at the Pb L<sub>1</sub>-edge (Figure 3). With longer solvothermal treatment time, the Fourier transform of the extended XAFS (FT-EXAFS) shows the nearest neighbor distance (Pb-Cl) decreasing in distance (Figure 3b). Fitting the EXFAS data to a cubic CsPbCl<sub>3</sub> structure works well for both the 0 and 2 h treatment times. The derived Pb-Cl bond lengths ( $d_{PbCl}$ ) for the 0 and 2 h samples are 2.856  $\pm$  0.023 and  $2.847 \pm 0.019$  Å, respectively, which is less than the expected  $d_{\rm PbCl}$  = 2.867 Å for the bulk material, as expected for substitutional doping. Satisfactory fits to a perfect cubic CsPbCl<sub>3</sub> structure could not be obtained for solvothermal

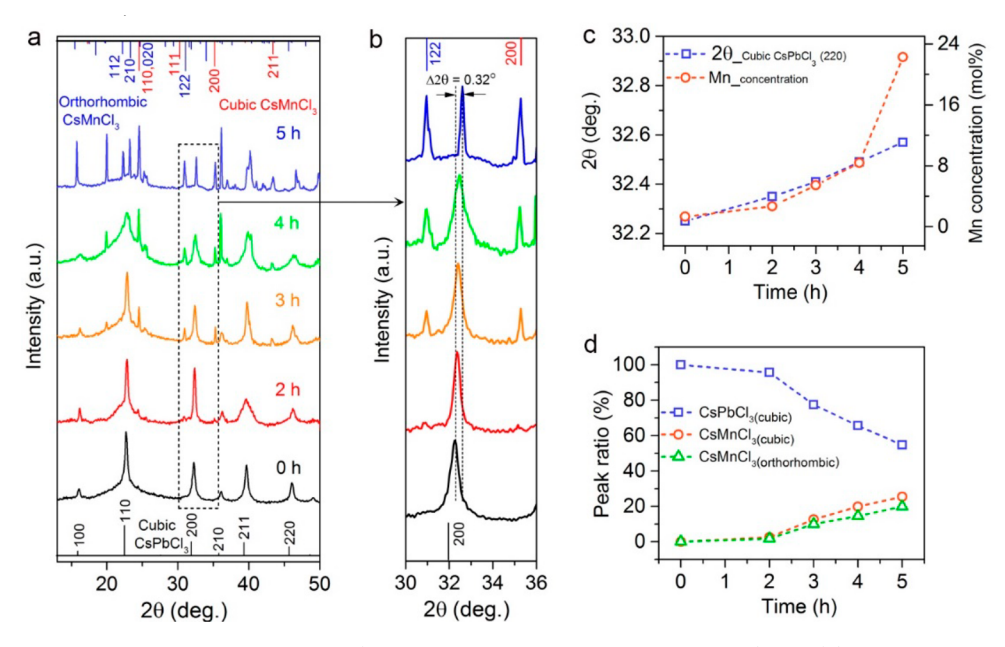


Figure 2. (a) XRD patterns of 2D Mn:CsPbCl<sub>3</sub> NPLs (using 80% Mn as precursor, mol % to Pb) and (b) a magnified view of the XRD peak around  $30^{\circ} \sim 36^{\circ}$  with different solvothermal treatment time. (c) Shift of the (200) XRD peak and dopant concentration as a function of solvothermal treatment time. (d) XRD intensity ratio of  $I_{CsPbCl3\_Cubic\ (200)}/I_{total}$ ,  $I_{CsMnCl3\_Cubic\ (200)}/I_{total}$ , and  $I_{CsMnCl3\_Orth\ (122)}/I_{total}$  as a function of solvothermal treatment time.

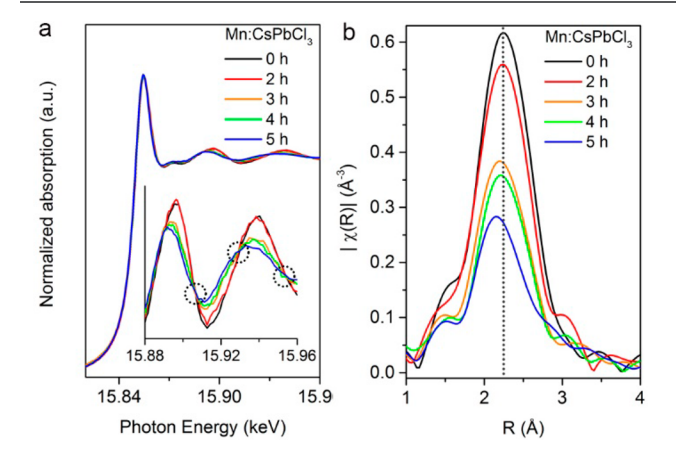


Figure 3. (a) XANES and (b) FT-EXAFS for the 2D  $Mn:CsPbCl_3$  NPLs as a function of solvothermal treatment time. The inset in (a) is an explanded region of the XANES spectra with the circles designating isosbestic points.

treatment times 3 h and greater, but modified cubic models (i.e., distorted octahedra) resulted in fair fit values ( $d_{3h} = 2.844 \pm 0.06$  Å and  $d_{5h} = 2.775 \pm 0.04$  Å). With increasing annealing time, the strong lattice distortions create larger variances in the Debye–Waller factors ( $\sigma_i$ ) making the EXAFS fitting less accurate. This is demonstrated by the broadening of the Pb–Cl scattering peak as time increases. In general, however, even neglecting the EXAFS fitting the gradual decrease of the main peak to lower R values in Figure 3b is consistent with a decreasing bond length, as the local environment is Cl and therefore any phase shift correction should be consistent. In addition, the amplitude of the Pb–Cl scattering peak decreases with longer solvothermal treatment time indicating the average coordination environment of Pb is decreasing, as expected for higher Mn doping levels.

Moreover, surprisingly, with increased doping concentration for longer solvothermal treatment time, two new XRD peaks at 30.9° and 35.3° gradually appear, which is consistent with the (122) and (200) lattice planes of orthorhombic CsMnCl<sub>3</sub> and cubic CsMnCl<sub>3</sub>, respectively (Figure 2b). The amount of the corresponding phases in the product could be estimated by analyzing the relative XRD peak intensities from the three phases. Compared to the 2D Mn:CsPbCl<sub>3</sub> NPLs before solvothermal treatment, the peak intensity ratio  $I_{CsPbCl3\ Cubic}$  $(200)/I_{total}$  ( $I_{total} = I_{CsPbCl3\_Cubic}$  (200) +  $I_{CsMnCl3\_Cubic}$  (200) +  $I_{CsMnCl3~Orth~(122)}$ ) gradually decreases from 100% to ~55% after 5 h solvothermal treatment, while the  $I_{CsMnCl3\_Cubic\ (200)}/I_{total}$ and  $I_{CsMnCl3~Orth~(122)}/I_{total}$  gradually increase from 0% to ~24% and ~21%, respectively (Figure 2d). Please note that the XRD intensity used in the calculation is normalized to their relative intensity for each phase; therefore, the peak intensity ratio between different phases could be used to qualitatively estimate the composition ratio in the NPLs considering the variation of XRD sample preparation and the anisotropic shape of the NPLs. This peak intensity ratio displays a trend of phase transition and segregation from Mn:CsPbCl3 NPLs to CsMnCl<sub>3</sub> NPLs, implying more Mn<sup>2+</sup> ions can replace the Pb<sup>2+</sup> sites in the CsPbCl<sub>3</sub> host and can even completely occupy all the Pb<sup>2+</sup> sites, leading to the formation of a new CsMnCl<sub>3</sub> phase during phase separation. It should be noted that during the solvothermal treatment no significant size or shape change was observed for the 2D NPLs (Figure 1c-d, Figure S1), confirming the phase segregation of Mn:CsPbCl<sub>3</sub> NPLs without any new nucleation event. This type of process, known as spinodal decomposition, refers to unmixing of components of solid solution from one thermodynamic phase to form two coexisting phases. 42 This spinodal decomposition mechanism is consistent with the X-ray absorption near edge structure (XANES) measurements (Figure 3a). Gradual changes in the multiple scattering peaks above the absorption threshold are observed, with the appearance of at least three isosbestic points (circles in Figure 3a). The appearance of

isosbestic points generally indicates a two-phase system, as suggested by the XRD measurements.

EPR spectroscopy was used to further confirm that Mn<sup>2+</sup> ions are doped into the Mn:CsPbCl<sub>3</sub> NCs (Figure 4). The X-

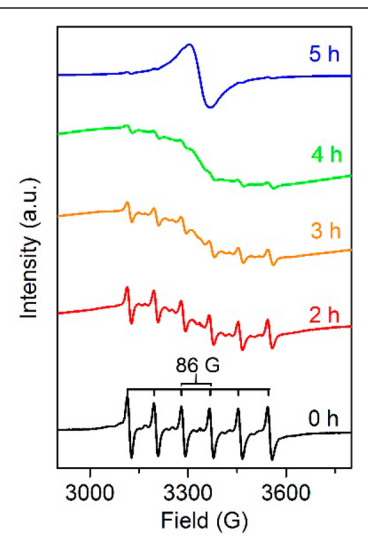


Figure 4. Room temperature X-band EPR spectra of 2D Mn:CsPbCl<sub>3</sub> NPLs with different solvothermal treatment times.

band EPR spectrum of the 2D Mn:CsPbCl<sub>3</sub> NPLs before solvothermal treatment shows a well-defined sextet hyperfine splitting pattern (hyperfine constant A = 86 G), which is the same value as the hyperfine constant observed in Mn-doped CsPbCl<sub>3</sub> NCs. 10,13,16 Upon the solvothermal treatment from 2 to 4 h, the EPR spectra of the 2D Mn:CsPbCl<sub>3</sub> NPLs exhibit a continuously broadening dipolar background with weakened hyperfine peaks. The broad dipolar background indicates the presence of short-range Mn-Mn interactions, which is consistent with higher Mn doping concentration for NPLs from longer solvothermal growth time (Figure 2c). 43-45 Further extending the solvothermal treatment time to 5.0 h leads to a new narrow dipolar peak from a pure CsMnCl<sub>3</sub> phase with short Mn-Mn interactions. The assignment of the narrow dipolar peak from a pure CsMnCl<sub>3</sub> phase was further confirmed by the EPR analysis of pure CsMnCl<sub>3</sub> phase synthesized in a control experiment by injecting cesium oleate solution into only the Mn precursor without any Pb present (Figures S2-S3), which shows similar broad EPR patterns to the 5 h growth sample shown in Figure 4. In addition, XRD and TEM data show the products are mainly cubic CsMnCl<sub>3</sub> with spherical morphology before solvothermal treatment, while the products gradually transfer to orthorhombic CsMnCl<sub>3</sub> without regular morphology after solvothermal treatment (Figure S2). This result is consistent with the gradual phase transition from the cubic to orthorhombic CsMnCl<sub>3</sub> obtained during solvothermal growth of Mn:CsPbCl3 NPLs.

Figure 5 shows the absorption and PL spectra of 2D Mn:CsPbCl<sub>3</sub> NPLs with different solvothermal treatment times. The 2D Mn:CsPbCl<sub>3</sub> NPLs before solvothermal treatment exhibit a first exciton absorption peak centered at 393 nm, which is blue-shifted compared to the band gap of bulk CsPbCl<sub>3</sub> (420 nm, 2.96 eV). This blue shift and sharp excitonic features in the absorption spectra clearly exhibit the quantum confinement of charge carriers in the 2D NPLs, which is attributed to the smaller thicknesses  $(3.0 \pm 0.3 \text{ nm})$  of

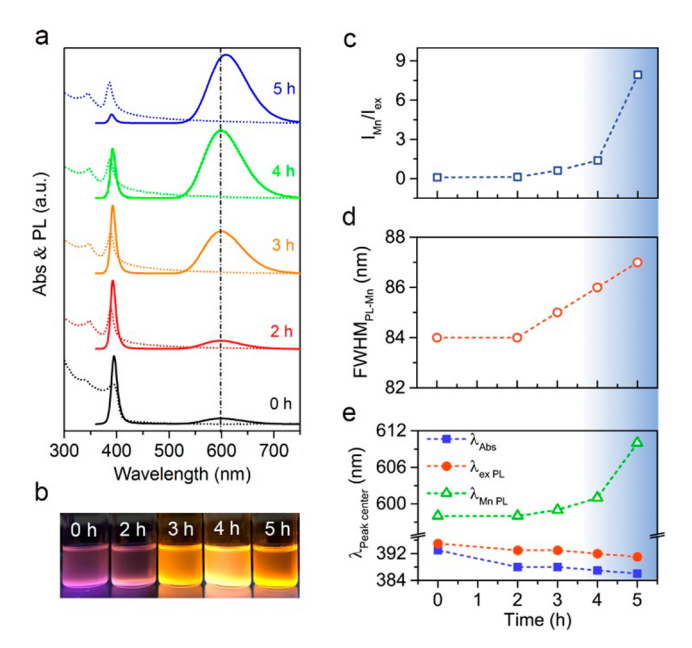


Figure 5. Optical properties of 2D Mn:CsPbCl<sub>3</sub> NPLs (using 80% Mn as precursor, mol % to Pb) under different solvothermal treatment time. (a) UV—vis absorption (dotted line) and PL spectra (solid line, with excitation at 350 nm) of 2D Mn:CsPbCl<sub>3</sub> NPLs. (b) Optical image of 2D Mn:CsPbCl<sub>3</sub> NPLs dispersed in toluene under UV (excitation at 365 nm) irradiation. (c) Intensity ratio of Mn emission to excitonic emission, (d) PL fwhm of Mn emission, and (e) peak center of lowest energy absorption peak ( $\lambda_{\rm Abs}$ ), host excitonic emission ( $\lambda_{\rm ex~PL}$ ), and Mn emission ( $\lambda_{\rm Mn~PL}$ ) as a function of the solvothermal treatment time.

the 2D Mn:CsPbCl<sub>3</sub> colloidal quantum well compared to the Bohr excitonic diameter of CsPbCl<sub>3</sub> (5 nm).<sup>47</sup>

The 2D Mn:CsPbCl<sub>3</sub> NPLs before solvothermal treatment exhibit a narrow host emission with full-width at half-maximum (fwhm) of ~12 at 395 nm, along with a weak and broad Mn PL band at ~598 nm (fwhm of 84 nm) attributed to the ligand field transition of Mn<sup>2+</sup> ions.<sup>48</sup> After solvothermal treatment, the relative intensity ratio of the Mn emission to the CsPbCl<sub>3</sub> host excitonic emission  $(I_{\rm Mn}/I_{\rm ex})$  increases gradually from 0.1 to 8.0 with increasing solvothermal treatment time (Figure 5c). Meanwhile, both the absorption and host PL peaks blue shift continuously from 393 to 386 nm and from 395 to 391 nm (Figure 5e), respectively, with longer solvothermal treatment. The blue shift is attributed to the lattice contraction, resulting from the replacement of larger Pb<sup>2+</sup> ions (133 pm) with smaller Mn<sup>2+</sup> ions (97 pm). <sup>15,17</sup> The lattice contraction results in shorter average Pb-Cl bonds and therefore stronger Pb-Cl orbital interactions, which can widen the band gap of Mndoped CsPbCl<sub>3</sub> NCs and blue shift the absorption spectra and host PL, as observed in Mn-doped CsPbCl<sub>3</sub> NCs previsously. 12,49 The continuous blue shift of the absorption and host PL peaks of the 2D Mn:CsPbCl3 NPLs is consistent with the increased Mn doping concentration, supported by ICP-OES analysis.

The 2D Mn:CsPbCl<sub>3</sub> NPLs before solvothermal treatment exhibit a relatively low Mn PL QY of  $\sim$ 2%. However, the Mn<sup>2+</sup> PL QY of 2D Mn:CsPbCl<sub>3</sub> NPLs increased dramatically with solvothermal treatment up to a maximum of  $\sim$ 21% for the 4.0 h sample, leading to a higher PL ratio of Mn PL and host CsPbCl<sub>3</sub> PL (Figure 5c) and an overall yellow-orange colored emission (Figure 5b). The Mn PL QY decreased to  $\sim$ 18% with

5 h solvothermal treatment, accompanying the phase transition to the CsMnCl<sub>3</sub> phase. The variation in QY of both the Mn and excitonic PL with solvothermal reaction time is shown in Table S2 and Figure S4. These results confirm that postsynthetic solvothermal treatment can promote the Mn diffusion and doping into the CsPbCl<sub>3</sub> lattice. In addition, gradual Mn PL peak broadening (Figure 5d) and red shifting (from 598 to 610 nm) (Figure 5e) can be observed, which could be understood by the multiple microenvironments for Mn dopant within Mn:CsPbCl<sub>3</sub> and CsMnCl<sub>3</sub> NPLs for longer solvothermal treatment.

To further reveal the dopant concentration- and phase-dependent optical properties, time-resolved emission measurements were conducted. The excitonic PL decay profiles of the 2D Mn:CsPbCl<sub>3</sub> NPLs display multiexponential decay for all samples, both before and after solvothermal treatment (Figure 6a). The average lifetime  $(\tau_{\rm ex})$  decreases dramatically (Figure

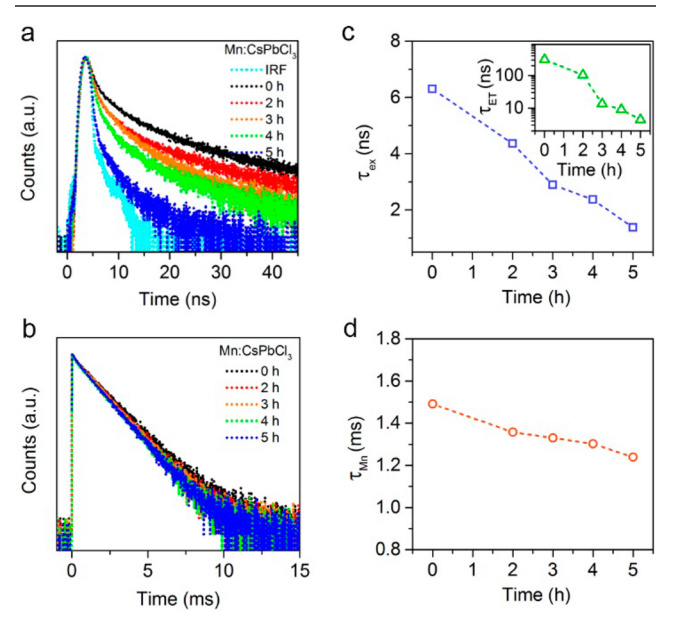


**Figure 6.** PL decays of (a) host exciton and (b)  $\mathrm{Mn^{2^+}}$  emission in 2D Mn:CsPbCl<sub>3</sub> NPLs as a fucntion of solvothermal treatment time (proportional to Mn concentration). (c) The host excitonic PL relaxation time (inset: energy transfer time) and (d) Mn emission relaxation time of 2D Mn:CsPbCl<sub>3</sub> NPLs as a function of solvothermal treatment time. The excitonic lifetime fits were deconvolved by the instrumental response function (IRF).

6c), from 6.3 to 1.4 ns, because of the increased energy transfer efficiency from host NPLs to  $Mn^{2+}$  ions with increased Mn incorporation (Figure 6a, Table S3). To gain an insight into the relative strength of the exciton–Mn exchange coupling, an approximation formula was employed to estimate the energy transfer time ( $\tau_{ET}$ ). <sup>16</sup>

$$QY_{Mn} = \left(\frac{k_{ET}}{k_{ex} + k_{ET}}\right) = \left(\frac{\frac{1}{\tau_{ET}}}{\frac{1}{\tau_{ex}} + \frac{1}{\tau_{ET}}}\right)$$
(1)

where  $QY_{Mn}$  is the Mn PL QY,  $k_{ET}$  is the energy transfer rate,  $k_{ex}$  is the radiative recombination rate constant of host excitons, and  $\tau_{ex}$  is the exciton relaxation time. The calculated energy transfer time  $\tau_{ET}$  of the 2D Mn:CsPbCl<sub>3</sub> NPLs decreased from 307.9 to 4.4 ns with increasing the solvothermal treatment time from 0 to 5 h, respectively

(Figure 6c inset). The energy transfer from exciton to Mn ions depends on the spatial overlap between the wave functions of the exciton and dopant ions. <sup>25,45,50,51</sup> The calculated results confirm that stronger exciton—Mn exchange coupling occurs with higher Mn doping concentration, leading to the increase in the energy transfer efficiency.

The decay curves of the Mn<sup>2+</sup> emission are shown in Figure 6b. The energy, peak width, and lifetime of the Mn emission are sensitive to the local lattice microenvironment on the doping site, which influences the strength of the ligand field of Mn<sup>2+</sup> ions as well as the vibronic coupling. <sup>45,51-53</sup> For the lower Mn concentrations (0-2 h), the Mn lifetime could be uniquely fitted to a single-exponential decay with a lifetime slightly decreased from 1.49 to 1.36 ms (Figure 6d, Table S3). The single-exponential decay of Mn PL lifetime suggests a nearly homogeneous environment of Mn dopants inside the CsPbCl<sub>3</sub> NPLs. 54,55 For NPLs with 3-4 h solvothermal treatment, the Mn lifetime could be fitted to either a singleexponential decay or two-exponential decays. However, for NPLs at higher Mn concentrations (for 5.0 h growth), the Mn PL decay becomes faster ( $\tau_{\rm Mn}$  decreases to 1.24 ms) and can only be fitted by multiple-exponential decay (Figure. 6d, Table S3), indicating the significant heterogeneity of the local doping environment. 54,55 Therefore, the broad Mn PL peak and nonexponential Mn PL decay were observed consistent with the coexistence of Mn:CsPbCl3 and CsMnCl3 phases, as the result of phase segregation. The concentration quenching significantly influences the excited Mn centers at this stage, resulting in decreased Mn PL lifetime and PL QY.

## DISCUSSION

In this study, higher Mn doping concentrations in CsPbCl<sub>3</sub> NPLs can be achieved by diffusion doping during a postsynthetic solvothermal process. Furthermore, it is intriguing to observe the new CsMnCl<sub>3</sub> phase formed by spinodal decomposition in the later stage of diffusion doping. It is believed that the fast ion diffusion under the solvothermal conditions facilitates the diffusion doping, leading to higher Mn doping efficiencies. When the doping concentration is above a certain threshold, phase separation can occur to release the strain generated by the large cationic size mismatch between Mn and Pb ions.

To further understand the effects of solvothermal conditions on the doping concentration and phase of the final NPLs, 2D Mn:CsPbCl<sub>3</sub> NPLs were also synthesized at 160 and 180 °C under solvothermal conditions (Figure 7, Figures S5-S10). TEM shows that the NPLs prepared at different solvothermal temperatures (160 and 180 °C) exhibit similar 2D morphology and size as NPLs obtained at 200 °C (Figure S5), which indicates that the reaction temperature does not significantly influence the growth of the host CsPbCl3 NPLs within the experimental temperature range. However, the Mn:CsPbCl<sub>3</sub> NPLs at 160 °C exhibited nearly identical emission profiles with similar intensity ratio of Mn emission to host excitonic emission regardless of solvothermal treatment time (Figure 7a). In addition, no notable change in the peak positions of the Mn or host excitonic emission, nor the Mn PL lifetime, was observed during solvothermal treatment process (Figure 7e, Figures S6-S7). ICP-OES analysis illustrates a similar Mn doping concentration (~2%) for the Mn:CsPbCl<sub>3</sub> NPLs synthesized at 160 °C (Table S1), with no phase separation/ transition observed from XRD (Figure S8). Interestingly, the NPLs obtained by solvothermal treatment at 180 °C displayed

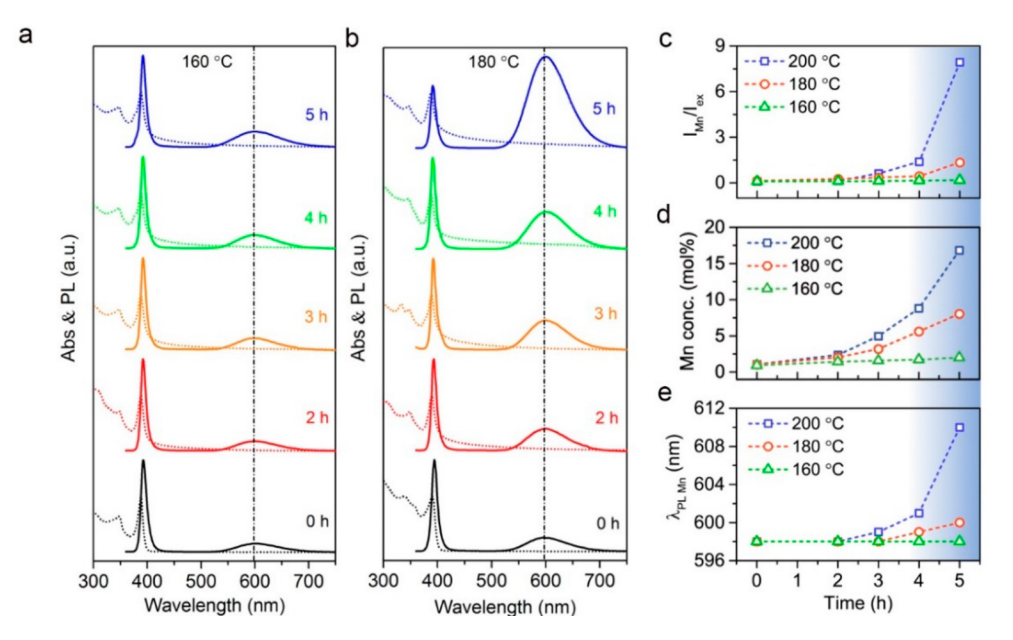


Figure 7. Comparison of optical properties of 2D Mn:CsPbCl<sub>3</sub> NPLs (using 80% Mn as precursor, mol % to Pb) under different solvothermal temperatures (160, 180, and 200 °C). (a, b) UV–vis absorption (dotted line) and PL spectra (solid line, with excitation at 350 nm) of 2D Mn:CsPbCl<sub>3</sub> NPLs obtained at 160 and 180 °C, respectively. (c) Intensity ratio of Mn emission to excitonic emission, (d) Mn doping concentration incorporated in NPLs, and (e) peak center of Mn emission as a function of solvothermal reaction time.

a change of PL, doping concentration, and phase that was intermediate between those of NPLs grown at 160 and 200 °C under solvothermal treatment (Figure 6, Figures S9–S10). For example, the ratio of Mn emission to excitonic emission slowly increased from 0.13 to 1.34 with increasing solvothermal treatment time (Figure 7b , c), while the Mn emission peak showed a slight red shift from 598 to 600 nm (Figure 7e). The Mn concentration increased from 0.8% to 8.0% for NPLs grown for 0 and 5 h, respectively, (Table S1) coupled with an increased Mn PL QY, up to a maximum of 10.2% for 5 h samples (Table S2, Figure S4). The new CsMnCl<sub>3</sub> phase was only observed for 5 h sample from XRD analysis (Figure S10).

Taken together, the diffusion-controlled doping under solvothermal conditions plays a critical role for the higher Mn doping efficiency and the formation of the new CsMnCl<sub>3</sub> phase by phase separation during the solvothermal treatment. The dependence of the phases and optical properties of the 2D NPLs on the solvothermal treatment temperature can be understood as a pressure (proportional to temperature) mediated process for dopant incorporation. It has been reported that the surface states and crystallography of materials alter significantly under sufficient pressure. Therefore, the rate of dopant diffusion, adsorption, and incorporation into the perovskite NPLs can be tuned by the temperature-dependent pressure under solvothermal conditions.

The experimental results indicate that the high temperatures (>160 °C), under solvothermal conditions, can facilitate ion diffusion and diffusion doping of Mn ions into the CsPbCl<sub>3</sub> without modifying the size and shape of the 2D NPLs. At relatively low Mn doping concentrations in Mn:CsPbCl<sub>3</sub> NPLs during the solvothermal treatment, the Mn<sup>2+</sup> doping environment ions are largely homogeneous, evidenced by the single-exponential decay of Mn PL. The increasing Mn concentrations can lead to higher Mn PL QY. While the efficient doping can be understood by the fast diffusion rate under solvothermal conditions, the phase separation is dependent on both doping concentration and reaction temperature. Gen-

erally, relatively high doping concentrations are required for phase separation during the solvothermal treatment. In addition, high temperature can also facilitate the phase separation. At 180 °C, a  $\sim$ 8% doping concentration is required for the phase separation, while at 200 °C the phase separation can occur with  $\sim$ 5% doping concentration.

While phase segregation from a uniform crystal via spinodal decomposition can occur in the bulk materials, the nanoinclusion inside doped NCs is very rare. In II-VI semiconductors quantum dots (QDs), incorporation of a dopant metal ion with the same charge (i.e., Mn(II), 59 Cr(II), 22 and Co(II))<sup>29</sup> leads to simple substitutional incorporation of the ion of interest up to its solubility limit. Incorporation of an ion that has a different charge, such as Cu(I),60 Cr(III),61 Eu(III),<sup>62</sup> Fe(III),<sup>63</sup> or Al(III),<sup>64</sup> results in formation of ion vacancies in the QD in order to reach charge neutrality, or in a rare case formation of ZnCr<sub>2</sub>Se<sub>4</sub> spinel inclusion inside Cr(III)-doped ZnSe QDs.<sup>65</sup> The unusual phase segregation in the 2D Mn:CsPbCl<sub>3</sub> NPLs could be understood by the flexible continuum model by considering the effects of coherency strains as well as the gradient energy term in the crystal lattice. 66,67 The strain is more significant with high Mn doping concentrations considering the large size mismatch (>30%) between the Mn<sup>2+</sup> (97 pm) dopant and the Pb<sup>2+</sup> (133 pm). However, the free energy can be lowered by allowing the components to separate, thus increasing the relative concentration of a component material in the spinodal region of the phase diagram. Therefore, phase separation can occur when the concentration of Mn dopant is too high and Mn:CsPbCl<sub>3</sub> NPLs transitions into the unstable region of the phase diagram.

The boundary of the unstable region can be found experimentally by determining the phases in temperature vs doping concentration diagram, as shown in Figure 8. Only Mn:CsPbCl<sub>3</sub> phase is present on the bottom-left part of the diagram with relatively low dopant concentration. As dopant concentration continues to increase, the Mn:CsPbCl<sub>3</sub> reaches the boundary of the phase diagram as indicated by the line on

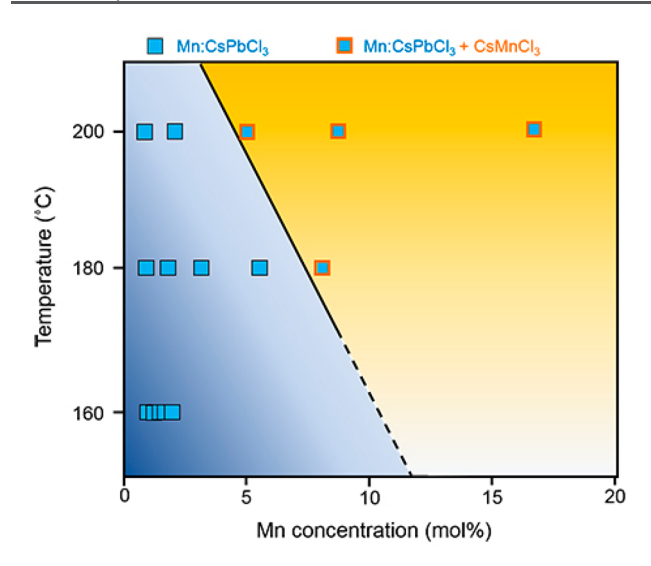


Figure 8. Phase diagram of  $Mn:CsPbCl_3$  NPLs under solvothermal conditions.

the diagram. Above the threshold of dopant concentration and solvothermal temperature, the Mn:CsPbCl<sub>3</sub> is moved into the spinodal region of the phase diagram so that spinodal decomposition can occur as observed in the right side of the phase diagram in Figure 8. During this spinodal decomposition, no new nucleation event occurs; therefore, no significant size and shape change was observed for the 2D NPLs under solvothermal conditions.

# CONCLUSION

In conclusion, we demonstrated a facile solvothermal method for efficient diffusion doping in 2D Mn:CsPbCl<sub>3</sub> NPLs and even the formation of a new CsMnCl<sub>3</sub> phase by spinodal decomposition without significantly altering the morphology and size of host perovskite NCs. ICP-OES, EPR, XAFS, and luminescence lifetime data confirm that the Mn doping efficiency was continuously improved during solvothermal treatment, while phase separation by spinodal decomposition can occur at later stage of diffusion doping, leading to the coexistence of Mn:CsPbCl3 and CsMnCl3 phases. The Mn doping efficiency and phase transition are strongly depending on the solvothermal reaction temperature and time, which further affects the optical properties of 2D Mn:CsPbCl<sub>3</sub> NPLs. The CsMnCl<sub>3</sub> inclusions by spinodal decomposition in Mndoped CsPbCl<sub>3</sub> NPLs are the first reported example of a nanoinclusion in isovalent doped NCs to the best of our knowledge. The ability to incorporate a new phase by spinodal decomposition provides a new understanding of doping inside quantum-confined NCs and a promising approach to study the interactions between the impurity and the host under moderate temperature and pressure.

#### EXPERIMENTAL SECTION

**Chemicals.** Cesium carbonate (Cs<sub>2</sub>CO<sub>3</sub>, 99.9% metals basis, Alfa Aesar), PbCl<sub>2</sub> (99.999%, Alfa Aesar), MnCl<sub>2</sub> (>99%, Aldrich), oleylamine (OAm, technical grade 70%, Aldrich), oleic acid (OA, technical grade 90%, Aldrich), 1-octadecene (ODE, technical grade 90%, Aldrich), toluene (ACS grade, VWR), and acetone (Certified ACS, VWR) were used as supplied.

**Preparation of Cesium Oleate Stock Solution.** A stock solution of cesium oleate (Cs(oleate)) was prepared followeing a reported method.<sup>47</sup> Briefly, Cs<sub>2</sub>CO<sub>3</sub> (130 mg), 1-octadecene (6.0

mL), and oleic acid (0.5 mL) were loaded into a 25 mL 3-neck round-bottom flask and dried under vacuum at 100 °C for 1 h. The mixture was then heated under argon at 140 °C until all  $Cs_2CO_3$  reacted with OA. The Cs(oleate) solution was stored at room temperature and was preheated to 140 °C just before use in perovskite 2D Mn:CsPbCl<sub>3</sub> NPLs synthesis.

Synthesis of Perovskite 2D Mn:CsPbCl<sub>3</sub> NPLs. 2D Mn:CsPbCl<sub>3</sub> NPLs were grown using a two-step process. In the first step, smaller 2D Mn:CsPbCl<sub>3</sub> NPLs were synthesized using a hotinjection method in long-chain capping ligands oleic acid and oleylamine. Subsequently, larger 2D Mn:CsPbCl<sub>3</sub> NPLs were formed by the assembly of corresponding smaller 2D Mn:CsPbCl<sub>3</sub> NPLs in a Teflon-lined stainless-steel autoclave under solvothermal condition.

a. Synthesis of Colloidal 2D Mn:CsPbCl<sub>3</sub> NPLs. The syntheses of smaller 2D Mn:CsPbCl<sub>3</sub> NPLs were performed by reacting Cs-oleate with PbCl<sub>2</sub> and MnCl<sub>2</sub> in ODE containing a mixture of long-chain capping ligands (OA and OAm). PbCl<sub>2</sub> (54 mg), MnCl<sub>2</sub> (20 mg), ODE (5.0 mL), OA (1.0 mL), and OAm (1.0 mL) were loaded into a 25 mL 3-neck flask and heated to 100 °C under vacuum for 30 min. Then the reaction mixture was refilled with argon and reacted for another 20 min at 120 °C. Subsequently, the Cs(oleate) (0.45 mL) was swiftly injected to form 2D Mn:CsPbCl<sub>3</sub> NPLs in 5–10 s. The solution was cooled down to room temperature by immersion in a water bath.

b. Growth of Larger Perovskite 2D Mn:CsPbCl $_3$  NPLs. The formed solution of smaller 2D Mn:CsPbCl $_3$  NPLs was transferred to an Arfilled glovebox and loaded into a 10 mL Teflon-lined autoclave without any purification. The autoclave was sealed and maintained at 200 °C for the required reaction time (1–5 h). The autoclave was then quickly cooled down to room temperature using an ice bath. Finally, the solution was transferred to a centrifuge tube and centrifuged at 5000 rpm for 5 min. The resulting larger 2D Mn:CsPbCl $_3$  NPLs were redispersed in 2 mL of toluene for further optical characterization.

For optical measurements, the samples were cleaned once by the centrifugation of the reaction solution at 5000 rpm for 5 min. The supernatant was discarded, and 1 mL toluene was added to redissolve the precipitate. For XRD measurements, the samples were cleaned at least two additional times to remove the excess ligand on the surface of the NCs. Briefly, 1 mL of toluene was added to redissolve the precipitate, and then 5 mL of acetone was added to precipitate the NCs by centrifuging at 5000 rpm for 5 min. This dissolution/reprecipitation process was repeated at least one more time to remove excess ligands. Finally, the NCs were dried under vacuum for XRD measurements.

**Sample Characterizations.** Transmission electron microscopy (TEM) measurements were performed on a FEI T12 Twin TEM operated at 120 kV with a LaB6 filament and Gatan Orius dual-scan CCD camera. Powder XRD patterns were taken on a Bruker D8 Advance powder diffractometer using Cu Kα radiation ( $\lambda = 1.5406$  Å). Inductively coupled plasma optical emission spectrometry (ICP-OES) for elemental analysis was performed on a PerkinElmer Optima 3300DV. For a standard ICP-OES measurement, the powdered samples were completely dissolved in 90% HNO<sub>3</sub>, heated to remove excess NO<sub>x</sub>, and then diluted to ~5 mL of ultrapure water. Room temperature electron paramagnetic resonance (EPR) spectra were recorded at a microwave frequency of 9.4 GHz on a BRU188 KER ELEXSYS-II ES00 spectrometer.

The UV—visible spectrophotometry (UV—vis) measurements were collected on an Agilent Cary 60 spectrophotometer. Steady-state and time-resolved emission spectroscopies were recorded using an Edinburgh FLS-980 spectrometer with a photomultiplier tube (PMT, R928 Hamamatsu) detector. For collection of steady-state emission spectra, the excitation wavelength was set to 350 nm, and a 360 nm long-wave pass optical filter was used to remove extraneous wavelengths from the excitation light. Time-resolved emission measurements were made by the time correlated single-photon counting (TCSPC) capability of the same instrument (FLS-980). For band gap emission measurement, the pulsed excitation light (365 nm) was generated by an Edinburgh EPL-365 pulsed laser diode operating

at a repetition rate of 0.2 MHz. The maximum emission channel count rate was less than 5% of the laser channel count rate, and each data set collected 5000 counts on the maximum channel. For Mn emission lifetime measurement, the pulsed excitation light (365 nm) was generated by a  $\mu$ F2 60 W xenon flashlamp operating at a repetition rate of 20 Hz. The detector signal was set below a threshold of 5000 counts per second. The lifetime of emission was determined by reconvolution fit with the instrument response function using the Edinburgh F980 software. In all cases, emission decay was satisfactorily fitted with a multiple-exponential function until reconvolution with goodness-of-fit ( $\chi_R^2$ ) in the range between 1.0 and 1.3.

X-ray absorption fine structure (XAFS) experiments were performed at Sector 10 on the insertion device line operated by the Materials Research Collaborative Access Team (MRCAT). Measurements were performed in fluorescence using a Lytle detector. Pellet samples consisting of the pure materials and BN were prepared and mounted perpendicular to the X-ray beam. Calibrations were done using a Pb foil for the Pb L<sub>1</sub>-edge. XAFS data processing and analysis were done using the IFEFFIT suite of programs. Initial estimates of the threshold energy values ( $E_0$ ) were obtained via the inflection point in the normalized absorption edges. A Hanning window was applied to a selected k-range (2–9 Å<sup>-1</sup>) to obtain the Fourier transformed extended XAFS (EXAFS) data. Using the bulk cubic CsPbCl<sub>3</sub> lattice as our fitting model, FEFF6 was used to calculate the photoelectron scattering path amplitudes,  $F_i(k)$ , and phase,  $\phi(k)$ , and the samples were fit to the EXAFS equation

$$\chi(k) = \frac{N_i S_o^2}{2kR_i^2} F_i(k) e^{-2k^2 \sigma_i^2} \sin[2kR_i + \phi_i(k)]$$

which allowed for the extraction of pertinent information including the bond lengths  $(R_i)$  and the EXAFS Debye–Waller factors (static disorders,  $\sigma_i^2$ ).

# ASSOCIATED CONTENT

#### Supporting Information

The Supporting Information is available free of charge on the ACS Publications website at DOI: 10.1021/acs.chemmater.8b02657.

Supplementary optical, XRD, and TEM data, control experiments, and data analysis (PDF)

#### AUTHOR INFORMATION

# **Corresponding Author**

\*E-mail: wzhen104@syr.edu.

ORCID 6

Weiwei Zheng: 0000-0003-1394-1806

Notes

The authors declare no competing financial interest.

#### ACKNOWLEDGMENTS

W.Z. acknowledges support from the start-up grant of Syracuse University. TEM measurements were performed at the Cornell Center for Materials Research (CCMR), which is supported through the NSF MRSEC program (DMR-1719875). ACERT is supported by the National Institutes of Health Grant NIH/NIBIB R010EB00315. W.Z. appreicates the valuble discussion on EPR with Prof. Kevin R. Kittilstved. W.Z. thanks Prof. Mathew M. Maye, Yuetian Chen, and Hediyeh Zamani for their help on the analysis of the size and thickness of the NPLs. We thank D. A. Driscoll at SUNY-ESF for help with ICP-OES measurements. The work at the University of Maine and Illinois Institute of Technology was supported by the National Science Foundation under Grant No. DMR-1708617. MRCAT

operations are supported by the Department of Energy and the MRCAT member institutions. Portions of this research used resources of the Advanced Photon Source, a U.S. Department of Energy (DOE) Office of Science User Facility operated for the DOE Office of Science by Argonne National Laboratory under Contract No. DE-AC02-06CH11357.

#### REFERENCES

- (1) Kovalenko, M. V.; Protesescu, L.; Bodnarchuk, M. I. Properties and potential optoelectronic applications of lead halide perovskite nanocrystals. *Science* **2017**, *358*, 745–750.
- (2) Lu, M.; Zhang, X.; Bai, X.; Wu, H.; Shen, X.; Zhang, Y.; Zhang, W.; Zheng, W.; Song, H.; Yu, W. W.; Rogach, A. L. Spontaneous silver doping and surface passivation of CsPbI<sub>3</sub> perovskite active layer enable light-emitting devices with an external quantum efficiency of 11.2%. ACS Energy Lett. 2018, 3, 1571–1577.
- (3) Li, J.; Xu, L.; Wang, T.; Song, J.; Chen, J.; Xue, J.; Dong, Y.; Cai, B.; Shan, Q.; Han, B.; Zeng, H. 50-Fold EQE improvement up to 6.27% of solution-processed all-inorganic perovskite CsPbBr<sub>3</sub> QLEDs via Surface ligand density control. *Adv. Mater.* **2017**, *29*, 1603885.
- (4) Waleed, A.; Tavakoli, M. M.; Gu, L.; Hussain, S.; Zhang, D.; Poddar, S.; Wang, Z.; Zhang, R.; Fan, Z. All inorganic cesium lead iodide perovskite nanowires with stabilized cubic phase at room temperature and nanowire array-based photodetectors. *Nano Lett.* **2017**, *17*, 4951–4957.
- (5) Sim, K. M.; Swarnkar, A.; Nag, A.; Chung, D. S. Phase stabilized  $\alpha$ -CsPbI<sub>3</sub> perovskite nanocrystals for photodiode applications. *Laser Photonics Rev.* **2018**, *12*, 1700209.
- (6) Swarnkar, A.; Marshall, A. R.; Sanehira, E. M.; Chernomordik, B. D.; Moore, D. T.; Christians, J. A.; Chakrabarti, T.; Luther, J. M. Quantum dot—induced phase stabilization of α-CsPbI<sub>3</sub> perovskite for high-efficiency photovoltaics. *Science* **2016**, *354*, 92–95.
- (7) Akkerman, Q. A.; Gandini, M.; Di Stasio, F.; Rastogi, P.; Palazon, F.; Bertoni, G.; Ball, J. M.; Prato, M.; Petrozza, A.; Manna, L. Strongly emissive perovskite nanocrystal inks for high-voltage solar cells. *Nat. Energy* **2017**, *2*, 16194.
- (8) Chen, S.; Shi, G. Two-dimensional materials for halide perovskite-based optoelectronic devices. Adv. Mater. 2017, 29, 1605449
- (9) Das Adhikari, S.; Dutta, A.; Dutta, S. K.; Pradhan, N. Layered perovskites  $L_2(Pb_{1-x}Mn_x)Cl_4$  to Mn-doped CsPbCl<sub>3</sub> perovskite platelets. ACS Energy Lett. **2018**, 3, 1247–1253.
- (10) Mir, W. J.; Jagadeeswararao, M.; Das, S.; Nag, A. Colloidal Mndoped cesium lead halide perovskite nanoplatelets. *ACS Energy Lett.* **2017**, 2, 537–543.
- (11) Yao, J.-S.; Ge, J.; Han, B.-N.; Wang, K.-H.; Yao, H.-B.; Yu, H.-L.; Li, J.-H.; Zhu, B.-S.; Song, J.-Z.; Chen, C.; Zhang, Q.; Zeng, H.-B.; Luo, Y.; Yu, S.-H. Ce<sup>3+</sup>-doping to modulate photoluminescence kinetics for efficient CsPbBr<sub>3</sub> nanocrystals-based light-emitting diodes. *J. Am. Chem. Soc.* **2018**, *140*, 3626–3634.
- (12) van der Stam, W.; Geuchies, J. J.; Altantzis, T.; van den Bos, K. H. W.; Meeldijk, J. D.; Van Aert, S.; Bals, S.; Vanmaekelbergh, D.; de Mello Donega, C. Highly emissive divalent-ion-doped colloidal CsPb<sub>1-x</sub>M<sub>x</sub>Br<sub>3</sub> perovskite nanocrystals through cation exchange. *J. Am. Chem. Soc.* **2017**, *139*, 4087–4097.
- (13) Zou, S.; Liu, Y.; Li, J.; Liu, C.; Feng, R.; Jiang, F.; Li, Y.; Song, J.; Zeng, H.; Hong, M.; Chen, X. Stabilizing cesium lead halide perovskite lattice through Mn(II) substitution for air-stable light-emitting diodes. *J. Am. Chem. Soc.* **2017**, *139*, 11443–11450.
- (14) Guria, A. K.; Dutta, S. K.; Adhikari, S. D.; Pradhan, N. Doping Mn<sup>2+</sup> in lead halide perovskite nanocrystals: successes and challenges. *ACS Energy Lett.* **2017**, *2*, 1014–1021.
- (15) Liu, H.; Wu, Z.; Shao, J.; Yao, D.; Gao, H.; Liu, Y.; Yu, W.; Zhang, H.; Yang, B. CsPb<sub>x</sub>Mn<sub>1-x</sub>Cl<sub>3</sub> perovskite quantum dots with high Mn substitution ratio. *ACS Nano* **2017**, *11*, 2239–2247.
- (16) Parobek, D.; Roman, B. J.; Dong, Y.; Jin, H.; Lee, E.; Sheldon, M.; Son, D. H. Exciton-to-dopant energy transfer in Mn-doped

cesium lead halide perovskite nanocrystals. *Nano Lett.* **2016**, *16*, 7376–7380.

- (17) Liu, W.; Lin, Q.; Li, H.; Wu, K.; Robel, I.; Pietryga, J. M.; Klimov, V. I. Mn<sup>2+</sup>-doped lead halide perovskite nanocrystals with dual-color emission controlled by halide content. *J. Am. Chem. Soc.* **2016**, *138*, 14954–14961.
- (18) Chen, D.; Fang, G.; Chen, X. Silica-coated Mn-doped CsPb(Cl/Br)<sub>3</sub> inorganic perovskite quantum dots: exciton-to-Mn energy transfer and blue-excitable solid-state lighting. *ACS Appl. Mater. Interfaces* **2017**, *9*, 40477–40487.
- (19) Lin, C. C.; Xu, K. Y.; Wang, D.; Meijerink, A. Luminescent manganese-doped CsPbCl<sub>3</sub> perovskite quantum dots. *Sci. Rep.* **2017**, 7, 45906.
- (20) Xu, K.; Lin, C. C.; Xie, X.; Meijerink, A. Efficient and stable luminescence from Mn<sup>2+</sup> in core and core—isocrystalline shell CsPbCl<sub>3</sub> perovskite nanocrystals. *Chem. Mater.* **2017**, *29*, 4265–4272.
- (21) Parobek, D.; Dong, Y.; Qiao, T.; Son, D. H. Direct hot-injection synthesis of Mn-doped CsPbBr<sub>3</sub> nanocrystals. *Chem. Mater.* **2018**, *30*, 2939–2944.
- (22) Zheng, W.; Kumar, P.; Washington, A.; Wang, Z.; Dalal, N. S.; Strouse, G. F.; Singh, K. Quantum phase transition from superparamagnetic to quantum superparamagnetic state in ultrasmall Cd<sub>1-x</sub>Cr(II)<sub>x</sub>Se quantum dots? *J. Am. Chem. Soc.* **2012**, *134*, 2172–2179.
- (23) Zheng, W.; Strouse, G. F. Involvement of carriers in the size-dependent magnetic exchange for Mn:CdSe quantum dots. *J. Am. Chem. Soc.* **2011**, *133*, 7482–7489.
- (24) Pradhan, N.; Peng, X. Efficient and color-tunable Mn-doped ZnSe nanocrystal emitters: control of optical performance via greener synthetic chemistry. *J. Am. Chem. Soc.* **2007**, *129*, 3339–3347.
- (25) Yang, Y.; Chen, O.; Angerhofer, A.; Cao, Y. C. Radial-position-controlled doping in CdS/ZnS core/shell nanocrystals. *J. Am. Chem. Soc.* **2006**, *128*, 12428–12429.
- (26) Harrigan, W. L.; Michaud, S. E.; Lehuta, K. A.; Kittilstved, K. R. Tunable electronic structure and surface defects in chromium-doped colloidal SrTiO<sub>3- $\delta$ </sub> nanocrystals. *Chem. Mater.* **2016**, 28, 430–433.
- (27) Mocatta, D.; Cohen, G.; Schattner, J.; Millo, O.; Rabani, E.; Banin, U. Heavily doped semiconductor nanocrystal quantum dots. *Science* **2011**, 332, 77–81.
- (28) Vlaskin, V. A.; Barrows, C. J.; Erickson, C. S.; Gamelin, D. R. Nanocrystal diffusion doping. *J. Am. Chem. Soc.* **2013**, *135*, 14380–14389.
- (29) Pittala, S.; Mortelliti, M. J.; Kato, F.; Kittilstved, K. R. Substitution of Co<sup>2+</sup> ions into CdS-based molecular clusters. *Chem. Commun.* **2015**, *51*, 17096–17099.
- (30) Sahu, A.; Kang, M. S.; Kompch, A.; Notthoff, C.; Wills, A. W.; Deng, D.; Winterer, M.; Frisbie, C. D.; Norris, D. J. Electronic impurity doping in CdSe nanocrystals. *Nano Lett.* **2012**, *12*, 2587–2594.
- (31) Eames, C.; Frost, J. M.; Barnes, P. R. F.; O'Regan, B. C.; Walsh, A.; Islam, M. S. Ionic transport in hybrid lead iodide perovskite solar cells. *Nat. Commun.* **2015**, *6*, 7497.
- (32) Nedelcu, G.; Protesescu, L.; Yakunin, S.; Bodnarchuk, M. I.; Grotevent, M. J.; Kovalenko, M. V. Fast anion-exchange in highly luminescent nanocrystals of cesium lead halide perovskites (CsPb $X_3$ , X = Cl, Br, I). *Nano Lett.* **2015**, *15*, 5635–5640.
- (33) Akkerman, Q. A.; D'Innocenzo, V.; Accornero, S.; Scarpellini, A.; Petrozza, A.; Prato, M.; Manna, L. Tuning the optical properties of cesium lead halide perovskite nanocrystals by anion exchange reactions. *J. Am. Chem. Soc.* **2015**, *137*, 10276–10281.
- (34) Bekenstein, Y.; Koscher, B. A.; Eaton, S. W.; Yang, P.; Alivisatos, A. P. Highly luminescent colloidal nanoplates of perovskite cesium lead halide and their oriented assemblies. *J. Am. Chem. Soc.* **2015**, *137*, 16008–16011.
- (35) Adhikari, S. D.; Dutta, S. K.; Dutta, A.; Guria, A. K.; Pradhan, N. Chemically tailoring the dopant emission in manganese-doped CsPbCl<sub>3</sub> perovskite nanocrystals. *Angew. Chem., Int. Ed.* **2017**, *56*, 8746–8750.

- (36) Zhai, W.; Lin, J.; Li, Q.; Zheng, K.; Huang, Y.; Yao, Y.; He, X.; Li, L.; Yu, C.; Liu, C.; Fang, Y.; Liu, Z.; Tang, C. Solvothermal synthesis of ultrathin cesium lead halide perovskite nanoplatelets with tunable lateral sizes and their reversible transformation into Cs<sub>4</sub>PbBr<sub>6</sub> nanocrystals. *Chem. Mater.* **2018**, *30*, 3714–3721.
- (37) Li, Z.-J.; Hofman, E.; Davis, A. H.; Maye, M. M.; Zheng, W. General strategy for the growth of  $CsPbX_3$  (X = Cl, Br, I) perovskite nanosheets from the assembly of nanorods. *Chem. Mater.* **2018**, *30*, 3854–3860.
- (38) Buonsanti, R.; Milliron, D. J. Chemistry of doped colloidal nanocrystals. *Chem. Mater.* **2013**, 25, 1305–1317.
- (39) Weidman, M. C.; Goodman, A. J.; Tisdale, W. A. Colloidal halide perovskite nanoplatelets: an exciting new class of semi-conductor nanomaterials. *Chem. Mater.* **2017**, *29*, 5019–5030.
- (40) Viswanatha, R.; Brovelli, S.; Pandey, A.; Crooker, S. A.; Klimov, V. I. Copper-doped inverted core/shell nanocrystals with "permanent" optically active holes. *Nano Lett.* **2011**, *11*, 4753–4758.
- (41) Swarnkar, A.; Mir, W. J.; Nag, A. Can B-Site doping or alloying improve thermal- and phase-stability of all-inorganic CsPbX<sub>3</sub> (X = Cl, Br, I) perovskites? *ACS Energy Lett.* **2018**, *3*, 286–289.
- (42) Alert, R.; Tierno, P.; Casademunt, J. Formation of metastable phases by spinodal decomposition. *Nat. Commun.* **2016**, *7*, 13067.
- (43) Nag, A.; Sapra, S.; Nagamani, C.; Sharma, A.; Pradhan, N.; Bhat, S. V.; Sarma, D. D. A Study of Mn<sup>2+</sup> doping in CdS nanocrystals. *Chem. Mater.* **2007**, *19*, 3252–3259.
- (44) Zheng, W.; Wang, Z.; Wright, J.; Goundie, B.; Dalal, N. S.; Meulenberg, R. W.; Strouse, G. F. Probing the local site environments in Mn:CdSe quantum dots. *J. Phys. Chem. C* **2011**, *115*, 23305–23314.
- (45) Li, Z.-J.; Hofman, E.; Blaker, A.; Davis, A. H.; Dzikovski, B.; Ma, D.-K.; Zheng, W. Interface engineering of Mn-doped ZnSe-based core/shell nanowires for tunable host—dopant coupling. *ACS Nano* **2017**, *11*, 12591—12600.
- (46) Akkerman, Q. A.; Motti, S. G.; Srimath Kandada, A. R.; Mosconi, E.; D'Innocenzo, V.; Bertoni, G.; Marras, S.; Kamino, B. A.; Miranda, L.; De Angelis, F.; Petrozza, A.; Prato, M.; Manna, L. Solution synthesis approach to colloidal cesium lead halide perovskite nanoplatelets with monolayer-level thickness control. *J. Am. Chem. Soc.* 2016, 138, 1010–1016.
- (47) Protesescu, L.; Yakunin, S.; Bodnarchuk, M. I.; Krieg, F.; Caputo, R.; Hendon, C. H.; Yang, R. X.; Walsh, A.; Kovalenko, M. V. Nanocrystals of cesium lead halide perovskites (CsPbX<sub>3</sub>, X = Cl, Br, and I): novel optoelectronic materials showing bright emission with wide color gamut. *Nano Lett.* **2015**, *15*, 3692–3696.
- (48) Pradhan, N.; Goorskey, D.; Thessing, J.; Peng, X. An alternative of CdSe nanocrystal emitters: pure and tunable impurity emissions in ZnSe nanocrystals. *J. Am. Chem. Soc.* **2005**, *127*, 17586–17587.
- (49) Brandt, R. E.; Stevanović, V.; Ginley, D. S.; Buonassisi, T. Identifying defect-tolerant semiconductors with high minority-carrier lifetimes: beyond hybrid lead halide perovskites. *MRS Commun.* **2015**, *5*, 265–275.
- (50) Chen, H.-Y.; Maiti, S.; Son, D. H. Doping location-dependent energy transfer dynamics in Mn-doped CdS/ZnS nanocrystals. *ACS Nano* **2012**, *6*, 583–591.
- (51) Hofman, E.; Robinson, R. J.; Li, Z.-J.; Dzikovski, B.; Zheng, W. Controlled dopant migration in CdS/ZnS core/shell quantum dots. *J. Am. Chem. Soc.* **2017**, *139*, 8878–8885.
- (52) Pradhan, N.; Das Adhikari, S.; Nag, A.; Sarma, D. D. Luminescence, plasmonic, and magnetic properties of doped semiconductor nanocrystals. *Angew. Chem., Int. Ed.* **2017**, *56*, 7038–7054.
- (53) Beaulac, R.; Archer, P. I.; van Rijssel, J.; Meijerink, A.; Gamelin, D. R. Exciton storage by Mn<sup>2+</sup> in colloidal Mn<sup>2+</sup>-doped CdSe quantum dots. *Nano Lett.* **2008**, *8*, 2949–2953.
- (54) Barthou, C.; Benoit, J.; Benalloul, P.; Morell, A. Mn<sup>2+</sup> concentration effect on the optical properties of Zn<sub>2</sub>SiO<sub>4</sub>: Mn phosphors. *J. Electrochem. Soc.* **1994**, *141*, 524–528.

(55) Vink, A. P.; de Bruin, M. A.; Roke, S.; Peijzel, P. S.; Meijerink, A. Luminescence of exchange coupled pairs of transition metal ions. *J. Electrochem. Soc.* **2001**, *148*, E313–E320.

- (56) Szafrański, M.; Katrusiak, A. Photovoltaic hybrid perovskites under pressure. J. Phys. Chem. Lett. 2017, 8, 2496–2506.
- (57) Schettino, V.; Bini, R. Constraining molecules at the closest approach: chemistry at high pressure. *Chem. Soc. Rev.* **2007**, *36*, 869–880
- (58) Postorino, P.; Malavasi, L. Pressure-induced effects in organic—inorganic hybrid perovskites. *J. Phys. Chem. Lett.* **2017**, *8*, 2613–2622.
- (59) Beaulac, R.; Schneider, L.; Archer, P. I.; Bacher, G.; Gamelin, D. R. Light-induced spontaneous magnetization in doped colloidal quantum dots. *Science* **2009**, *325*, 973–976.
- (60) Knowles, K. E.; Hartstein, K. H.; Kilburn, T. B.; Marchioro, A.; Nelson, H. D.; Whitham, P. J.; Gamelin, D. R. Luminescent colloidal semiconductor nanocrystals containing copper: synthesis, photophysics, and applications. *Chem. Rev.* **2016**, *116*, 10820–10851.
- (61) Lehuta, K. A.; Haldar, A.; Zhou, D.; Kittilstved, K. R. Spectroscopic study of the reversible chemical reduction and reoxidation of substitutional Cr ions in Sr<sub>2</sub>TiO<sub>4</sub>. *Inorg. Chem.* **2017**, *56*, 9177–9184.
- (62) Raola, O. E.; Strouse, G. F. Synthesis and characterization of Eu-doped cadmium selenide nanocrystals. *Nano Lett.* **2002**, *2*, 1443–1447.
- (63) Brozek, C. K.; Zhou, D.; Liu, H.; Li, X.; Kittilstved, K. R.; Gamelin, D. R. Soluble supercapacitors: large and reversible charge storage in colloidal iron-doped ZnO nanocrystals. *Nano Lett.* **2018**, 18, 3297–3302.
- (64) Buonsanti, R.; Llordes, A.; Aloni, S.; Helms, B. A.; Milliron, D. J. Tunable infrared absorption and visible transparency of colloidal aluminum-doped zinc oxide nanocrystals. *Nano Lett.* **2011**, *11*, 4706–4710.
- (65) Zheng, W.; Singh, K.; Wang, Z.; Wright, J. T.; van Tol, J.; Dalal, N. S.; Meulenberg, R. W.; Strouse, G. F. Evidence of a ZnCr<sub>2</sub>Se<sub>4</sub> spinel inclusion at the core of a Cr-doped ZnSe quantum dot. *J. Am. Chem. Soc.* **2012**, *134*, 5577–5585.
- (66) Cahn, J. W. On spinodal decomposition. *Acta Metall.* **1961**, *9*, 795–801.
- (67) Cahn, J. W. On spinodal decomposition in cubic crystals. *Acta Metall.* **1962**, *10*, 179–183.
- (68) Ravel, B.; Newville, M. ATHENA, ARTEMIS, HEPHAESTUS: data analysis for X-ray absorption spectroscopy using IFEFFIT. *J. Synchrotron Radiat.* **2005**, *12*, 537–541.